Progress in Medical Devices
ISSN: 2957-5478

Zentime

Research Article https://doi.org/10.61189/409228vdbtgj

Design and experimental study of novel plasma ablation electrodes

Siqi Zhao[1], Lin Mao[1], Chengli Song[1], Zhuotianhao Wang[2]

[1]Shanghai Institute for Minimally Invasive Therapy, School of Health Science and Engineering, University of Shanghai for Science and Technology, Shanghai 200093, China. [2]Department of Biology, Shenzhen MSU-BIT University, Shenzhen 518000, Guangdong Province, China.

Corresponding author: Lin Mao.

Declaration of conflict of interest: None.

Received October 23, 2024; Accepted January 21, 2025; Published June 30, 2025

Highlights

- Three different electrode structures, including ring-needle electrode, needle electrode, and cylinder electrode, were designed to accommodate diverse surgical requirements.
- A novel low-temperature plasma ablation electrode features interchangeable tips, enabling surgeons to select appropriate tips based on specific operative situations.
- With increased electric field strength, ring-needle electrodes facilitates liquid medium breakdown, thereby opti mizing plasma generation and ablation efficacy.

Abstract

Objective: This study utilizes finite element modeling to investigate the coupled electric-thermal field distributions for three novel electrode designs, assessing their ability to induce electric breakdown in saline for plasma generation. Furthermore, the ablation effects of various electrode shapes were validated through ex vivo tissue ablation experiments, ensuring both the safety and feasibility of the electrodes. **Methods**: Three electrode structures were designed: the ring-needle electrode, the needle electrode, and the cylinder electrode. A COMSOL Multiphysics finite element model simulated their behavior in saline. This modeling approach enabled a detailed analysis of the spatial variations in both the electric and temperature fields. Furthermore, the electrodes were tested at four voltages (180 V, 220 V, 260 V, and 300 V) and a frequency of 100 kHz on porcine liver tissue to evaluate ablation performance. **Results**: Simulations showed temperatures of 25-70 °C at 0.3 mm above the three electrodes, with electric field strength exceeding 1 *10^6 V/m, which are sufficient to trigger electric breakdown and plasma formation. Ex vivo experiments confirmed ablation efficacy, with the ring-needle electrode exhibited the best performance at a voltage of 300 V, achieving a 2.3 mm ablation depth and 0.72 mm^2 thermal damage area. **Conclusion**: Finite element simulation and ex vivo experiments demonstrate the feasibility of the proposed electrodes, highlighting their potential as an innovative solution for plasma-based ablation technologies.

Keywords: Low-temperature plasma, ablation electrode, structural design, Multiphysics simulation

Introduction

Tonsils, or palatine tonsils, are lymphoid tissues located in the upper oropharyngeal and nasopharyngeal regions, serving a crucial immunological function in infection defense. In clinical practice, patients may experience varying degrees of pharyngeal pain, which may significantly impair both physical and psychological well-being, ultimately affecting their overall quality of life. Therefore, prompt and effective intervention is crucial to mitigate these adverse effects [1]. For patients with chronic pharyngeal inflammation secondary to recurrent acute tonsillitis, peritonsillar abscesses, or tonsillar hypertrophy-induced obstructive sleep apnea, symptom severity dictates the necessity for immediate treatment. Cases demonstrating severe symptoms require urgent medical attention. Appropriate therapeutic intervention must be implemented promptly to minimize adverse health impacts and maintain quality of life. Un-

Address correspondence to: Lin Mao, Shanghai Institute for Minimally Invasive Therapy, School of Health Science and Engineering, University of Shanghai for Science and Technology, NO.516 Jungong Road, Yangpu District, Shanghai 200093, China. Tel: +86-21-55572159. E-mail: linmao@usst.edu.cn.

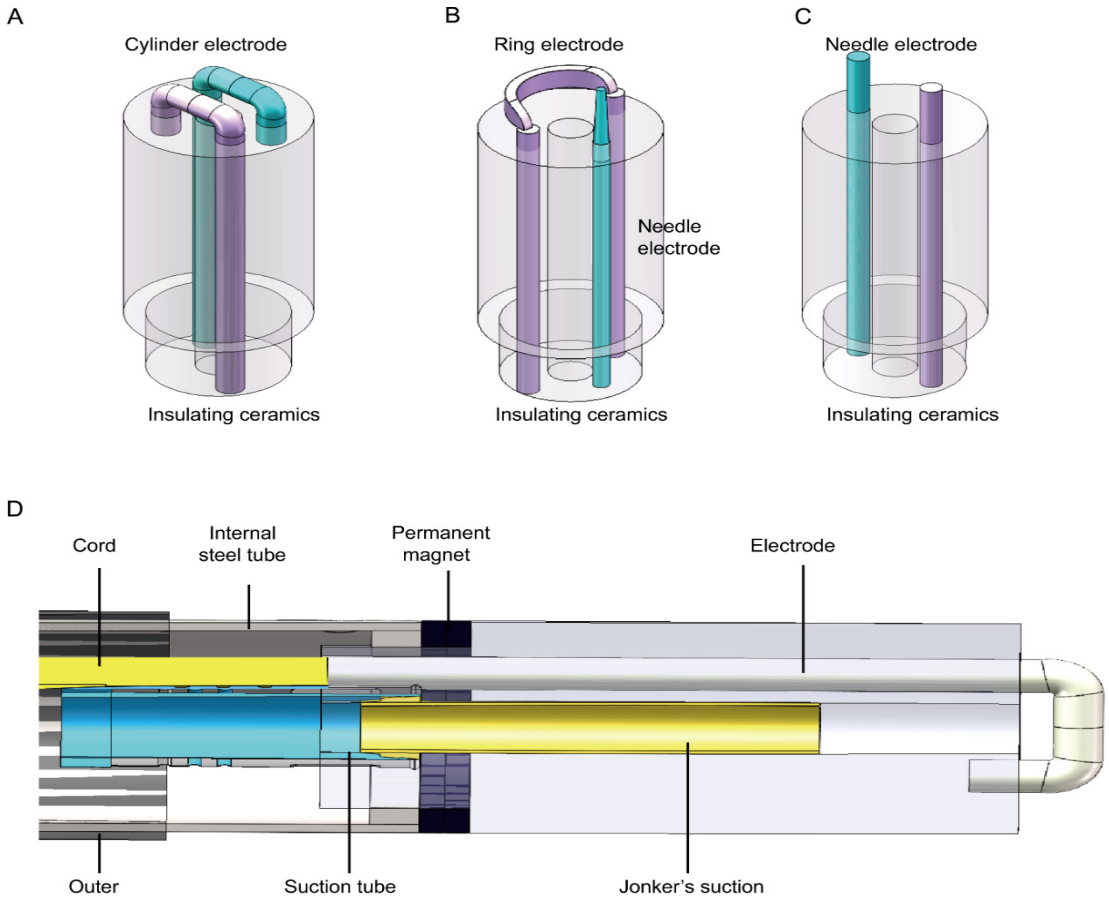

Figure 1. Three-dimensional model of a low-temperature plasma ablation tip. (A) Cylinder electrode; (B) Ring-needle electrode; (C) Needle electrode; (D) Detailed structural view of the ablation head.

der clinical supervision, tonsillectomy may represent a more effective treatment option over conservative management [2].

In otolaryngological practice, tonsillectomy techniques are classified into two categories: cold dissection (conventional surgical excision) and thermal methods employing high-frequency electrosurgery [3, 4]. Currently, electric surgical tools widely used in medical practice, such as high-frequency instruments, function by generating resistive heat during current passage through electrodes to achieve tissue sectioning. This significant thermal mechanism frequently induces substantial collateral tissue damage, potentially compromising wound healing and promoting excessive scar formation [5-8]. Conversely, traditional scalpel-based procedures are often associated with significant postoperative pain due to their mechanical cutting action. Furthermore, cold knife surgery lacks inherent hemostatic property, potentially increasing both intraoperative and postoperative hemorrhage, thereby requiring supplementary hemostatic measures [9-11].

Recent advances have introduced low-temperature plasma ablation technology as a minimally invasive alternative that overcomes limitations of conventional techniques regarding surgical precision, hemorrhage control, and thermal injury. This technology facilitates precise dissection and efficient coagulation through small incisions, offering distinct advantages including reduced postoperative discomfort, faster recovery, improved hemostasis, and decreased thermal damage compared to traditional methods [12-16]. These characteristics demonstrate the significant clinical potential and promising applications of low-temperature plasma technology in surgical practice.

China has made significant strides in the field of low-temperature plasma ablation scalpel technology, with research primarily concentrating on liquid-phase plasma generation [17, 18]. Key developments include multi-channel drainage circulation systems and optimized suction ports. Current plasma scalpel designs integrate anti-clogging mechanisms and ensure uniform saline coverage of electrodes. Notably, significant advancements have been made in liquid injection systems, which facilitate stable plasma layer formation while providing effective

cooling and cleaning of ablation sites. However, previous studies have primarily focused on innovative suction and irrigation systems to minimize electrode-induced thermal damage. Less attention has been paid to issues such as non-replaceable cutter heads and the monomorphic emitter electrode designs. These design constraints prevent surgical adaptation to varying operative conditions, potentially compromising ablation efficacy - an issue requiring urgent investigation. Electrode design must carefully balance thermal damage minimization with surgical effectiveness, considering both surgical outcomes and patient safety.

Precise control of plasma scalpel thermal effects is essential to prevent collateral tissue damage. Empirical evidence indicates that optimized electrode structural design, along with the fine-tuning of plasma parameters, can significantly contribute to the precise temperature control and the mitigation of unintended thermal injury [19, 20]. Finite Element Modeling and Finite Element Analysis serve as potent tools within the biomedical domain, they facilitate an in-depth investigation of electrothermal field variations and foster the development of novel technologies [21, 22]. By employing COMSOL Multiphysics, we conducted an in-depth analysis of the coupled thermal - electrical interactions of various electrode configurations in physiological saline, yielding essential theoretical data for assessing system stability and safety.

Materials and methods

3D models

A three-dimensional model of the low-temperature plasma ablation head was developed, as depicted in **Figure 1**. This model is primarily comprised of a titanium electrode head, an insulating ceramic component, and essential ancillary devices. The present study introduces three distinct electrode configurations: the cylinder electrode (**Figure 1A**), the ring-needle electrode (**Figure 1B**), and the needle electrode (**Figure 1C**), each fabricated from titanium. These electrodes feature one side electrically grounded and the opposing side serving as the anode. The design incorporates insulated permanent magnets at the proximal ends of both the ceramic head and inner steel tube. These magnets are arranged with opposing polarities, ensuring secure attachment to the scalpel handle through magnetic coupling, as illustrated in **Figure 1D**.

Physical model control equations

Finite element analysis was performed using the COMSOL Multiphysics (COMSOL, UK) to investigate the coupling between electromagnetic and thermal fields. The simulation incorporated the 'Electric Currents' and 'Heat Transfer in Solids' modules for multiphysics coupling. The electric field distribution was governed by fundamental electromagnetic principles:

Current continuity described by Ohm's law ($J=\sigma E$), where J represents current density (A/m^2), σ denotes conductivity (S/m), and E is electric field intensity (V/m) [23];

Electrostatic field distribution following the Laplace equation: $\nabla \cdot(\sigma \nabla V)=0$ [24];

Electric field-potential relationship: . $E=-\nabla V$

The thermal field was modeled using the heat transfer equation [25]:$\rho C \partial T/\partial t- \nabla\cdot(k \nabla T)=J\cdot E$. In this context, T represents the temperature (°C), ρ denotes the mass density (kg/m^3), C indicates the specific heat capacity (J/(kg*K)), t refers to time (s), and J·E accounts for Joule heating.

Material properties

The electrothermal characteristics of plasma generation in saline were analyzed using COMSOL 6.0. Material parameters were selected according to simulation requirements, with key properties listed in **Table 1**. The temperature-dependent saline properties were derived from empirical equations, where T represents the real-time temperature (°C) [26, 27].

Simulation models and boundary conditions

To optimize computational efficiency, the original saline model was simplified to a cylindrical structure. This streamlined model reduces computational complexity, accelerates calculation speed, while preserving model accuracy, enabling faster simulations with lower computational costs. A detailed schematic of the simplified model is presented in **Figure 2A**.

Boundary conditions were defined for both the contact surface between the geometric model and the surrounding environment, and the internal contact surface within the model. It is necessary to add a potential boundary condition and a ground boundary condition for the current (ec). Specifically, in the simulation of the ring-needle electrode, one side was assigned a positive potential, while the opposite side was grounded. The global parameters, as indicated in **Table 1**, were set to 260 V. Addi-

Table 1. Material properties

Position	Materials	Displayed formula	Value	Properties
Ceramic Glass	rho_GI	2595 [kg/m^3]	2595 kg/m^3	Densities, Ceramic Glass
	k_GI	1.09 [W/(m*K)]	1.09 W/(mK)	Thermal conductivity, Ceramic Glass
	Cp_GI	750 [J/(kg*K)]	750 J/(kgK)	Heat capacity, Ceramic Glass
	sigma_GI	1e-5 [S/m]	1E-5 S/m	Electrical conductivity, Ceramic Glass
Electrode	rho_Ti	4500 [kg/m^3]	4500 kg/m^3	Densities, Titanium
	k_Ti	21.90 [W/(m*K)]	21.90 W/(mK)	Thermal conductivity, Titanium
	Cp_Ti	523 [J/(kg*K)]	523 J/(kgK)	Heat capacity, Titanium
	sigma_Ti	2.5e5 [S/m]	2.5E5 S/m	Electrical conductivity, Titanium
	V0	260 [V]	260 V	Initial voltage
	T0	19.85 [deg C]	293 K	Initial temperature

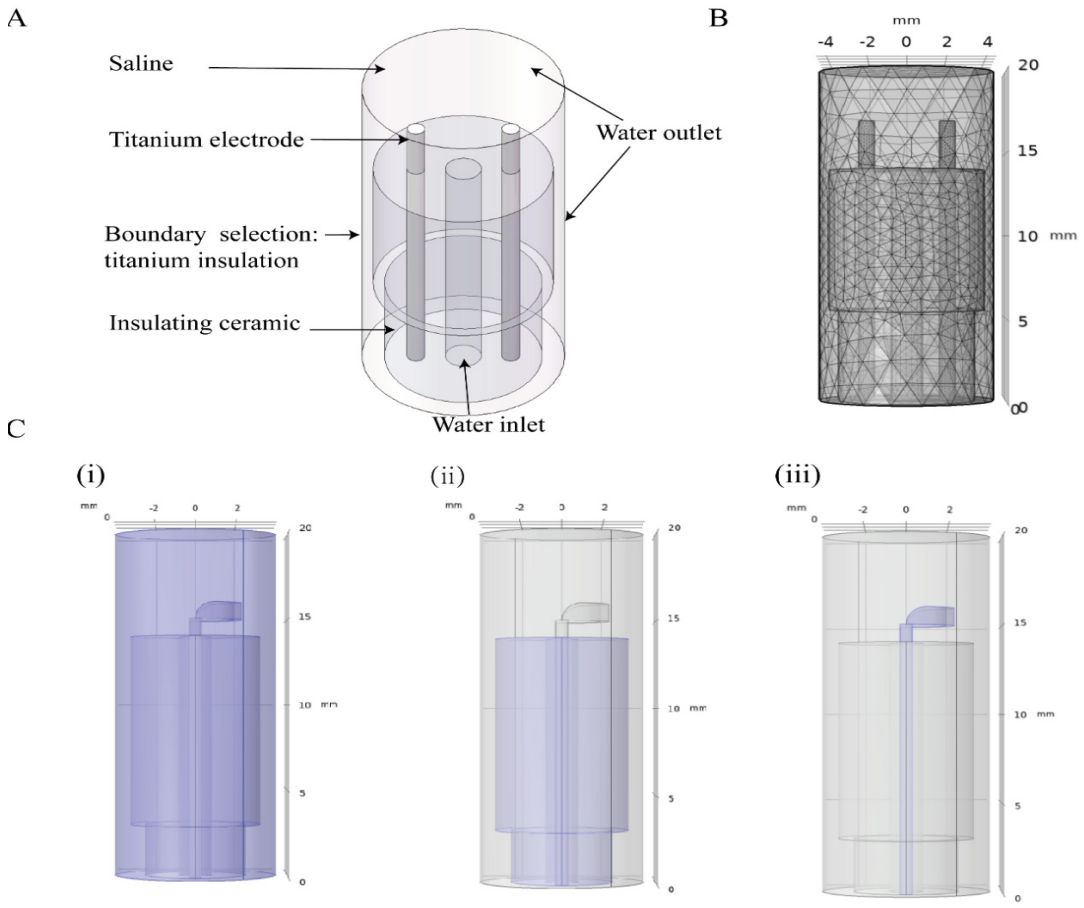

Figure 2. Simulation model and its specific parameter settings. (A) Simplified model of the electrode tip; (B) 3D meshing diagram of the model; (C) Electrode boundary geometric entity layers: electrode (i); insulating ceramic (ii); physiological saline (iii).

tionally, the surface in contact with the physiological saline and the external environment was designated as electrically insulating. In terms of solid heat transfer, the initial temperature was set to 293 K, as shown in **Table 1**, with the boundary conditions illustrated in **Figure 2C**.

To balance accuracy and computational efficiency, the grid size was optimized, and the model was discretized into tetrahedral meshes. A needle electrode was selected as a representative model for the simulation. The geometry included four domains, 26 boundaries, 44 edges, and 28 vertices. The mesh consisted of 102,482 domain elements, 10,412 boundary elements, and 752 edge elements. **Figure 2B** depicts a 3D diagram of the generated mesh. The coupled electric-thermal fields were solved using transient time stepping, employing PARDISO direct solver for the simulation [28].

Electrode ablation experiment

Three different electrode tip configurations were fabricated using 3D printing technology and subsequently assembled. Discharge and

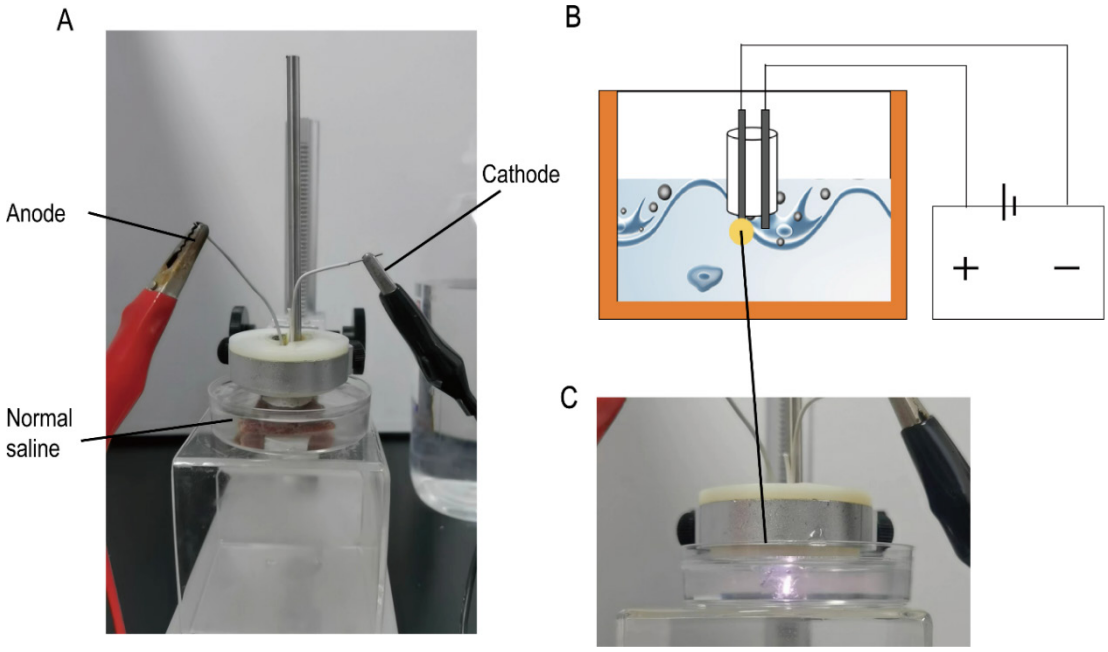

Figure 3. Discharge and ablation experiments. (A) Physical diagram; (B) Schematic diagram; (C) Detailed diagram.

ablation experiments were performed in physiological saline at various voltage levels, with the experimental setup shown in **Figure 3**.

At standard temperature and pressure, discharge measurements were conducted on plasma equipment connected to the same electrode at different voltage levels: 180 V, 220 V, 260 V, and 300 V, and the observed phenomena were documented. Simultaneously, the discharge characteristics of plasma equipment with differently structured electrodes were measured at the same voltage levels. A total of 12 photographs were taken to illustrate the experimental phenomena, with particular emphasis on the generation of orange plasma at varying voltages. Due to variations in electrode shapes, the voltage required for stable plasma generation differed among plasma devices. Voltages of 180 V, 220 V, 260 V, and 300 V were applied, and ablation of porcine liver tissue was performed at these voltage levels. To compare the ablation effects of the three electrodes, the ablation process was carried out at four distinct voltages. In total, four sets of experiments were conducted for electrodes with different shapes, resulting in 12 experimental sets.

Results

Temperature field simulation of the 3D electrode model

The temperature field simulation results for three electrodes are shown in **Figures 4A-C**. The temperature of the physiological saline, in regions distal to electrodes, exhibited slight fluctuations over time, maintaining a stable value of 19.85 °C. Notably, the temperature increased around the electrode as the distance decreases, reaching a maximum of 110.298 °C for the needle electrode (**Figure 4A**). The peak temperature in the ring-needle electrode simulation was approximately 106°C (**Figure 4B**), while the peak temperature of the cylinder electrode was 94 °C (**Figure 4C**). Temperature variations were examined at a distance of 0.3 mm above the electrodes. For the needle electrode (**Figure 4D**), the temperature of the physiological saline gradually increased over time. At time t = 1E-5, the temperature 0.3 mm above the needle electrode ranged from 20 °C to 110 °C, with higher temperatures observed near the electrode and temperatures remaining below 40 °C further away. For the ring-needle electrode (**Figure 4E**), a noticeable temperature gradient was observed in a localized area centered around the electrode. These results suggest a concentration of thermal energy near the electrode tips, which may influence tissue interaction and ablation effectiveness. At time t = 1E-5, the temperature of the physiological saline near the electrode peaked at approximately 100°C, while temperatures in the surrounding regions dropped slightly below 35 °C. As depicted in Figure 4F, the temperature near the cylinder electrode gradually escalated before reaching a plateau, with a range of approximately 32 °C to 47 °C.

Electric field simulation of the 3D electrode model

The one-dimensional electric field distributions for three electrode configurations are shown in **Figures 5A-C**. This simulation study investigates

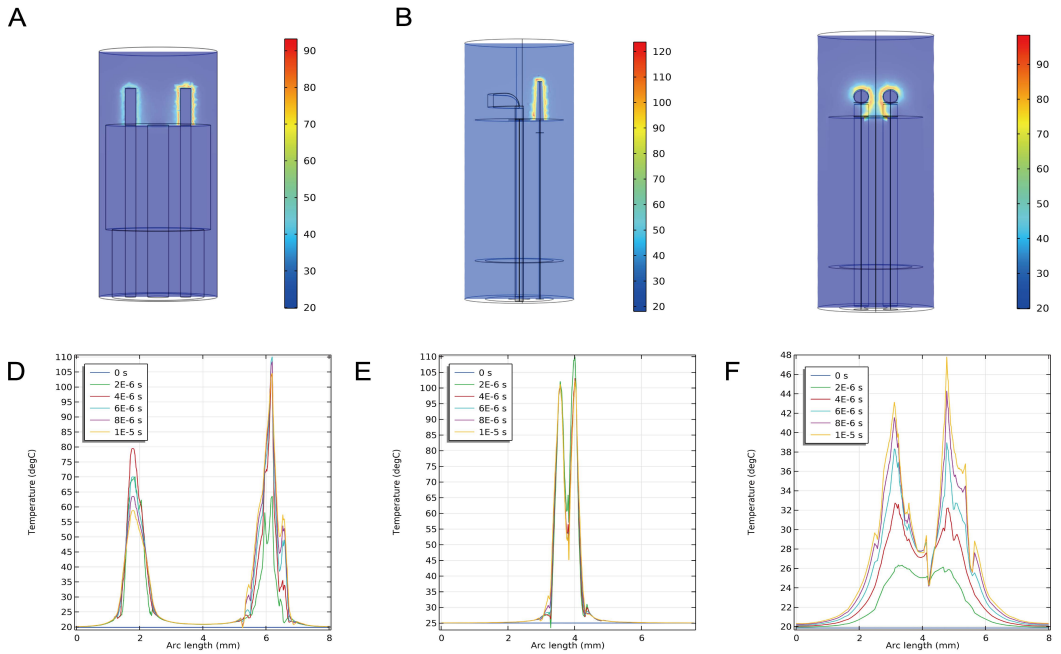

Figure 4. Temperature field simulation of different electrodes and the temperature variation curve over time at 0.3 mm above different electrodes. (A) Needle electrode; (B) Ring-needle electrode; (C) Cylinder electrode; (D) Needle electrode; (E) Ring-needle electrode; (F) Cylinder electrode.

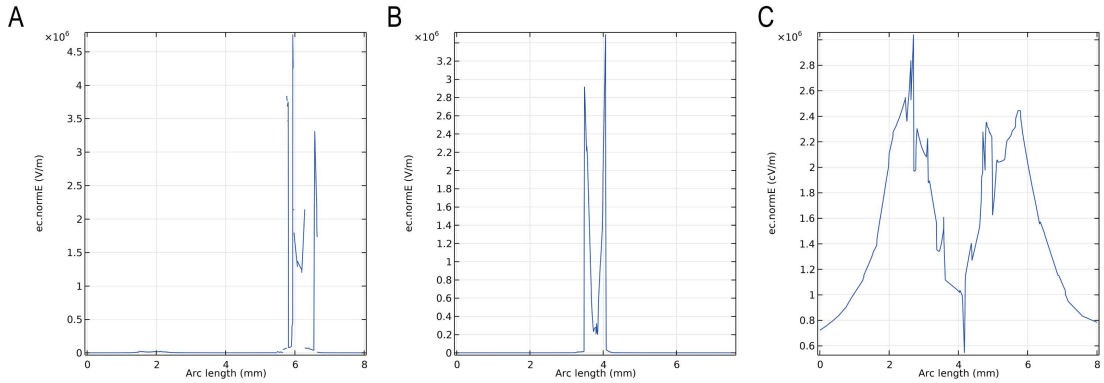

Figure 5. One-dimensional diagram of the electric field distribution for different electrode discharging in physiological saline. (A) Needle electrode; (B) Ring-needle electrode; (C) Cylinder electrode.

the correlation between electric field intensity and arc length, with a particular focus on field strength variations along the discharge path.

As shown in **Figure 5A**, the field strength in the central region of the needle electrode reached 1.57*10^6 V/m, meeting the minimum plasma formation threshold. **Figure 5B** illustrates the one-dimensional electric field model of the ring-needle electrode. The field strength in the central ring region was 1.2*10^6 V/m, while the field strength in most discharge areas of the electrode exceeded 1.8*10^6 V/m, and the maximum field strength reached 3.4*10^6 V/m. For the cylinder electrode, as shown in **Figure 5C**, the field strength near the electrode was 1.6*10^6 V/m. Notably, the field strength exceeded the 1*10^6 V/m threshold in majority regions. A comparative analysis of the one-dimensional electric field distribution images for the three electrode configurations under identical voltage and temperature conditions reveals that the local electric field intensity of the ring-needle electrode was markedly higher than that of the needle and cylinder electrodes.

Electrode ablation experiment

The discharge properties of the electrode were systematically examined across a range of voltages. **Figure 6A** illustrates the electrodischarge phenomena observed for the needle electrode at four distinct voltage levels (180 V, 220 V, 260 V, and 300 V). In **Figure 6A(i)**, it is evident that no orange substance was generated. **Figures 6A(ii-iii)** demonstrate that at volt-

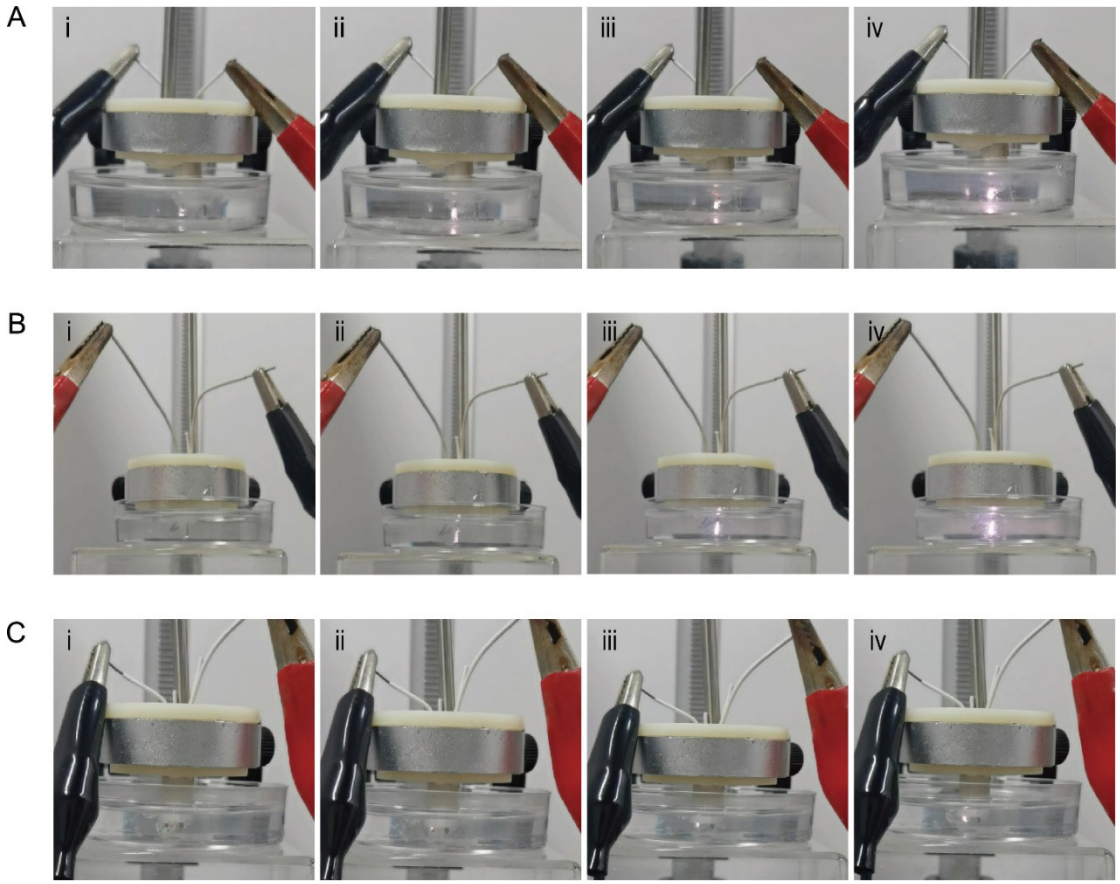

Figure 6. Discharge behavior of three types of electrodes in saline solution at different voltages. (A) Needle electrode; (B) Ring-needle electrode; (C) Cylinder electrode; i-iv: 180 V, 220 V, 260 V, and 300 V.

ages of 220 V and 260 V, orange substances, identified as plasma, were generated, although the color remains relatively dark. **Figure 6A(iv)** reveals that at 300 V, the electrode produced a stable bright orange substance. As the voltage increasing, the effects of the needle electrode became increasingly pronounced (**Figure 6B**). Experimental results indicate that at 300 V, the orange plasma light emitted by the needle electrode reached its maximum brightness. **Figure 6C** shows that while the intensity of the orange discharge from the cylinder electrode augmented with increasing voltage, it remained lower compared to the needle electrode, even at the highest voltage tested. Among the four voltage levels evaluated, the cylindrical electrode exhibited the most favorable discharge characteristics at 300 V. A comparative longitudinal analysis of the discharge phenomena for the three distinct electrode types, as depicted in **Figures 6A(iv), 6B(iv), and 6C(iv)**, indicates that the ring-needle electrode generated an orange-colored discharge material with the highest luminosity. This is followed by the needle electrode, which exhibits a comparatively lower luminosity, while the cylinder electrode demonstrates the least luminosity among the three.

Building on this foundation, a detailed analysis was conducted on the electrode ablation effects under varying voltage conditions. **Figure 7A** shows the thermal damage area and effective ablation depth from a 2-second needle electrode ablation of porcine liver tissue. As the voltage increased from 180 V to 260 V, the effective ablation depth increased rapidly from 0.4 mm to 1.7 mm. However, from 260 V to 300 V, the depth of the effective ablation area experienced a deceleration, increasing only from 1.7 mm to 2.1 mm. The effective ablation area was significantly enlarged at this voltage level, while the thermal damage to surrounding normal tissue was relatively minimized. **Figure 7B** delineates that at a voltage of 300 V, the ring-needle electrode yielded the smallest thermal damage area, measured at 0.72 mm^2, and the deepest effective ablation, reaching 1.13 mm in depth. Furthermore, **Figure 7C** illustrates that with increasing voltage, there was a corresponding reduction in the thermal damage area associated with cylinder electrode ablation, suggesting an optimization of the ablation process at higher voltages. At 180 V, the thermal damage area reached its maximum. Although the effective ablation depth increased with voltage, the increase was minimal, with a change of only 0.7 mm.

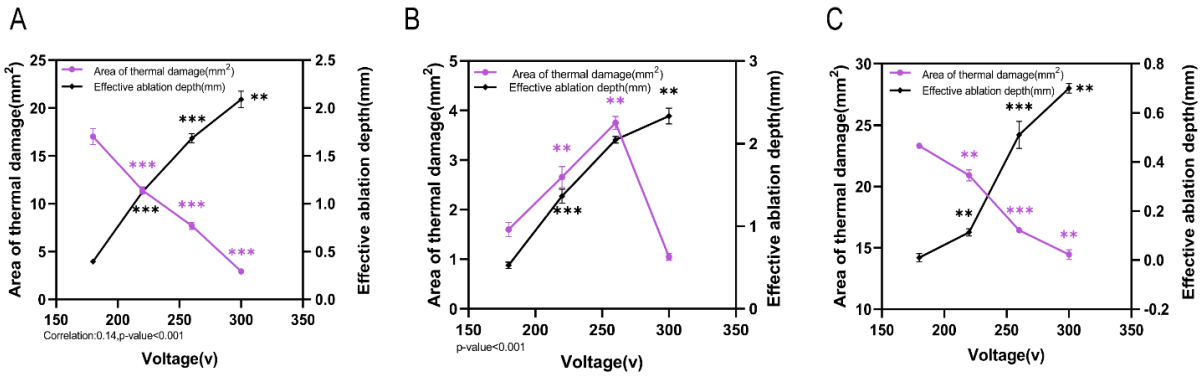

Figure 7. Curves showing the change in thermal injury area and effective ablation depth in porcine liver tissue over time for different electrodes. (A) Needle electrode; (B) Ring-needle electrode; (C) Cylinder electrode.

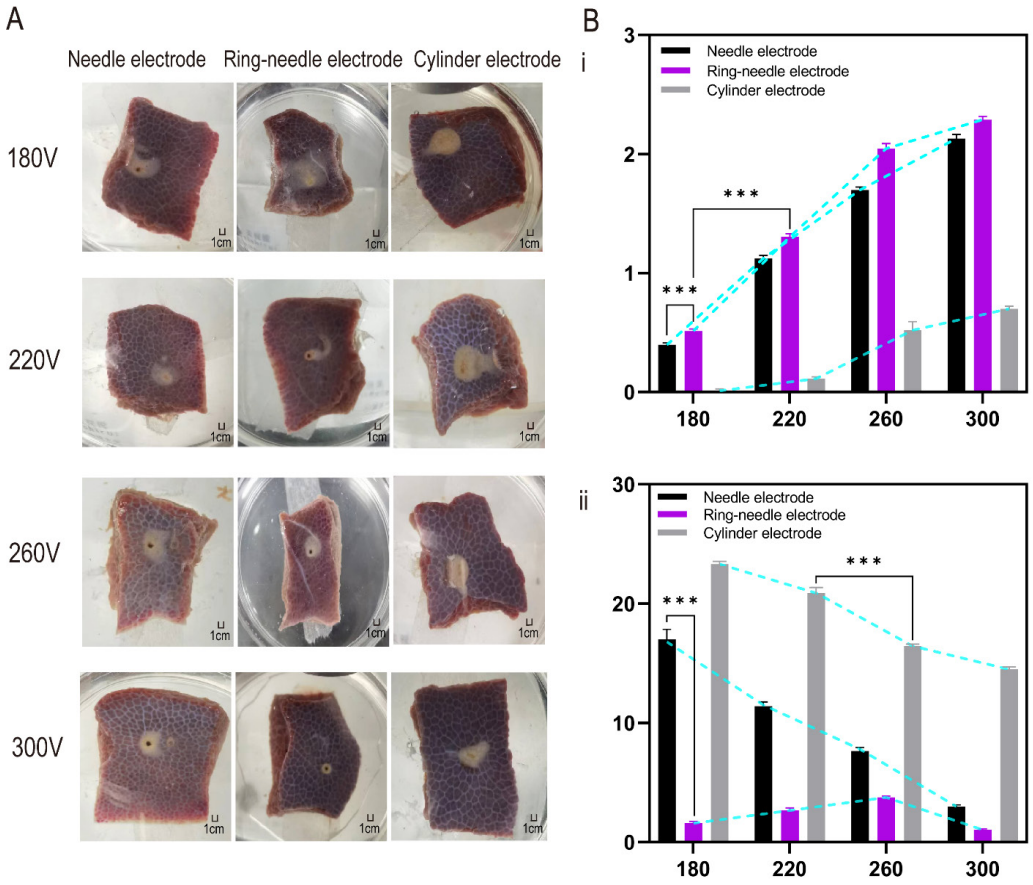

Figure 8. Voltage-dependent ablation effects of three types of electrodes. (A) Pictures of ablation effects on porcine liver tissue from three types of electrodes; (B) Curves of effective ablation depth (i) and thermal damage area (ii) for three types of electrodes.

This study systematically evaluates the ablation performance of three electrode configurations under standardized voltage conditions. Comparative analysis of ablation effects (**Figure 8A**) reveals a consistent efficacy hierarchy: ring-needle electrodes demonstrate superior performance, followed by needle electrodes, with cylinder electrodes exhibiting the lowest efficacy. Specifically, at the maximum test voltage of 300 V, the ring-needle electrode exhibited the smallest area of protein denaturation and discoloration, significantly lower than that observed with the needle and cylinder electrodes. The voltage-dependent ablation characteristics are presented in **Figure 8B**. Both ablation depth and thermal damage area exhibit non-linear relationships with applied voltage. As voltage increasing, the effective ablation depth in porcine liver tissue increased for all three electrodes, ranked from largest to smallest as follows: ring-needle type electrode, needle type electrode, and cylinder electrode (**Figure 8B(i)**). Furthermore, **Figure 8B(ii)** indicates that, with increasing voltage, the thermal damage area for both the needle and cylinder electrodes exhibited a gradual reduction. In contrast,

ring-needle electrode demonstrated an initial increase in thermal damage with subsequent decrease. A comprehensive analysis of **Figures 8A-B** reveals that the ring-needle electrode results in reduced thermal damage and a larger ablation area at the same voltage.

Discussion

Low-temperature plasma ablation represents a significant advancement in tissue ablation technology, integrating cutting, hemostasis, and suction capabilities while maintaining a low-temperature condition. This methodology offers multiple clinical benefits, including reduced postoperative inflammation, minimized patient discomfort, improved surgical field visualization, and enhanced procedural efficiency. These advantages have established low-temperature plasma ablation in tonsillectomy surgery as an increasingly important tool in tonsillectomy procedures, with growing recognition of its clinical value [14]. While existing research has primarily focused on optimizing plasma layer formation and implementing rapid cooling/cleaning mechanisms through multi-channel drainage systems, critical limitations in current device design have remained unaddressed. The fixed configuration of conventional plasma scalpel heads, featuring non-replaceable electrodes with uniform emission geometries, presents significant constraints in adapting to diverse surgical requirements. In this study, three distinct electrodes configurations were designed to address the aforementioned issue.

The simulation results demonstrate distinct thermal gradients surrounding the three electrode types, with proximal temperatures reaching 70-100 °C while rapidly decreasing with distance from the electrode surface. This finding confirms the localized effect of low-temperature plasma ablation, where the elevated temperatures are confined to the immediate tissue interface while maintaining sub-lethal temperatures in surrounding regions. This temperature range not only facilitates effective ablation but also minimizes thermal injury to adjacent tissues. Through extensive research and precise calculations, significant results have been achieved in temperature distribution, and accurate simulations of the electric field distribution have been demonstrated. According to the dielectric breakdown theory of gas discharge ignition, when the electric field intensity within the vapor layer exceeds a certain critical threshold, the gaseous medium in the vapor layer undergoes electrical breakdown, leading to electron avalanche ionization and the formation of plasma [29]. The electric field intensity E within the vapor layer can be rigorously expressed as: $E = \frac{U_V}{l_V}$,where l_V is the thickness of the vapor layer, and U_V is the voltage applied across the electrodes. Plasma discharge in saline liquid media involves complex vapor-layer dynamics and localized electric field distributions. The breakdown threshold is determined based on the properties of the gas mixture. In this study, the vapor layer primarily consists of a mixture of hydrogen and water vapor, and the breakdown field strength of the vapor layer is set to an empirical value of 1*10^6 V/m. This empirical value is commonly used to describe the breakdown behavior of air or similar gases (e.g., water vapor, hydrogen, etc.), with the specific magnitude determined based on factors including the ionization energy of the gas molecules, collision cross-section, and dielectric properties of the gas mixture [30]. In the experiment, the applied voltages (180 V, 220 V, 260 V, and 300 V) were combined with the corresponding vapor layer thicknesses to calculate the resulting electric field strengths. These values were then compared to the empirical breakdown threshold ($1*10^6$ V/m) to validate whether the breakdown conditions were satisfied.

Image analysis revealed that the three electrode structures designed in this study were capable of generating bubble layer with thickness ranging from 100 to 300 μm in saline medium, as determined by finite element analysis. Within these bubble layers, the electric field strength exceeded 1*10^6 V/m, sufficient to induce electrical breakdown and ensure plasma formation, thereby establishing favorable conditions for subsequent experiments.

The discharge phenomena of cylinder electrode in the saline solution under four different voltages were not significant. This indicates that at this stage, only minimal plasma was generated, primarily causing thermal damage through heating. Notably, in sparse discharge regions, such localized heating can readily lead to tissue burns [14].

A comprehensive study was conducted on the ablation effects of electrodes with different shapes under the same voltage conditions. The results indicate that the effective ablation depth decreases as follows: ring-needle, needle, and cylinder electrodes. Bio-thermal damage is determined by the combined effect of temperature and exposure time. When the cumulative thermal dose exceeds a critical threshold, the affected tissue is deemed to have undergone thermal necrosis [31, 32]. For

instance, at 300 V, the ring-needle electrode demonstrated the smallest area of protein denaturation and discoloration, indicating the least thermal damage to surrounding healthy tissue. Concurrently, as voltage increased, the thermal damage area decreased for both needle and cylinder electrodes. This trend may be attributed to enhanced electric field intensity at higher voltages, which triggers electrical breakdown and subsequent plasma generation. When employing the ring-needle electrode for ablation of porcine liver tissue, the thermal damage area initially increased and then decreased. This observation suggests that as voltage rises, both the quantity of generated plasma and its energy content also increase. Therefore, higher voltage correlates with enhanced ablation capability and improved resection efficacy. However, it should be noted that while increasing voltage can expand the effective ablation zone, exceeding a certain threshold may result in more severe thermal damage to surrounding normal tissue. Hence, the application of higher voltages in clinical practice requires cautious consideration.

This study comprehensively investigated the mechanical design, finite element simulation, and ablation experiments of three types of electrodes. However, long-term studies remain necessary to confirm their safety and efficacy, particularly regarding whether the electrodes can reliably generate plasma discharges in saline environments. If the findings are extended to low-temperature plasma ablation procedures for tonsillectomy, we can anticipate that both the needle and ring needle electrodes would demonstrate satisfactory temperature and electric field distributions to meet clinical requirements. A significant challenge lies in the performance of cylinder electrodes. Specifically, when ablating porcine liver tissue, the cylinder electrode failed to achieve effective plasma-mediated ablation, resulting in substantial thermal damage. This failure can be attributed to insufficient electric field strength, not reaching the threshold required for electrical breakdown, which inhibits plasma generation. Potential causes for this phenomenon include insufficient extension length of the cylinder electrode and/or incomplete contact between the bipolar cutting surface and the tissue. Additionally, different types of material processing require distinct plasma characteristics, which in turn affect the plasma discharge process and its characteristics [33]. To address this issue, potential solutions include optimizing electrode length, adjusting electrode geometry, and modifying the conductive properties of electrode material to promote more stable and intense plasma generation, thereby increasing plasma yield. Furthermore, the effects of different voltage levels on the discoloration area and effective ablation depth can help determine optimal voltage parameters.

Conclusion

Through finite element simulation analysis and ablation experiments involving three distinct electrode shapes, the feasibility and advantages of each electrode were validated. The findings indicate that all three electrodes can effectively achieve tissue cutting and ablation during surgical procedures while significantly minimizing thermal damage to adjacent normal tissues. Furthermore, these electrodes generate vapor layers where the electric field intensity is sufficient to induce electrical breakdown, thereby facilitating plasma formation. Experimental results demonstrate that as the voltage increases, the electrodes produce brighter and more stable plasma. Notably, at 300 V, all three electrodes generated the most stable and luminous plasma. Additionally, as the voltage increases, thermal damage to surrounding normal tissue decreases, while the effective ablation area expands. Among the tested electrodes, the ring-needle electrode demonstrated the highest ablation efficiency.

In summary, these three electrodes can effectively achieve tissue cutting and hemostasis while ensuring the safety of therapeutic outcomes. This research provides a novel approach for the design of electrodes for low-temperature plasma ablation, thereby promoting their medical applications and clinical development.

Author Contributions: Chengli Song, Lin Mao and Siqi Zhao conceived this project. Chengli Song and Siqi Zhao carried out structural design and finite element simulation. Lin Mao and Chengli Song designed an electrode ablation experiment. Siqi Zhao and Zhuotianhao Wang performed experiments and collected the relevant data and analyzed. All the authors contributed to the writing of manuscript, with Lin Mao making important contributions throughout the research and writing process.

References

[1] Harris E. Tonsillectomy Effective for People With Frequent Sore Throats. JAMA 2023;329(23):2011-2011.

[2] Wilson JA, O'Hara J, Fouweather T, et al. Conservative management versus tonsillectomy in adults with recurrent acute

tonsillitis in the UK (NATTINA): a multicentre, open-label, randomised controlled trial. Lancet 2023;401(10393):2051-2059.
[3] Kandemir S, Pamuk AE, Özel G, et al. Comparison of Three Tonsillectomy Techniques: Cold Dissection, Monopolar Electrocautery, and Coblation. Int Arch Otorhinolaryngol 2023;27(04):e694-e698.
[4] Subaşı B, Oğhan F, Taşlı H, et al. A comparison of the harmonic scalpel, coblation, bipolar, and cold knife tonsillectomy methods in adult patients. J Surg Med 2021;5(12):1198-1201.
[5] Zhong Y, Wei Y, Min N, et al. Comparative healing of swine skin following incisions with different surgical devices. Ann Transl Med 2021;9(20):1514.
[6] Dandu N, Nelson BB, Easley JT, et al. Quantifying the magnitude of local tendon injury from electrosurgical transection. J Shoulder Elbow Surg 2022;31(4):832-838.
[7] Lacitignola L, Desantis S, Izzo G, et al. Comparative Morphological Effects of Cold-Blade, Electrosurgical, and Plasma Scalpels on Dog Skin. Vet Sci 2020;7(1):8.
[8] Chang EI, Carlson GA, Vose JG, et al. Comparative Healing of Rat Fascia Following Incision with Three Surgical Instruments. J Surg Res 2011;167(1):e47-e54.
[9] Clark CM, Schubart JR, Carr MM. Trends in the management of secondary post-tonsillectomy hemorrhage in children. Int J Pediatr Otorhinolaryngol 2018;108:196-201.
[10] Haq AU, Bansal C, Pandey AK, et al. Analysis of Different Techniques of Tonsillectomy: An Insight. Indian J Otolaryngol Head Neck Surg 2022;74(3):5717-5730.
[11] Lieberg N, Aunapuu M, Arend A. Coblation tonsillectomy versus cold steel dissection tonsillectomy: a morphological study. J Laryngol Otol 2019;133(9):770-774.
[12] Karthik C, Sarngadharan SC, Thomas V. Low-Temperature Plasma Techniques in Biomedical Applications and Therapeutics: An Overview. Int J Mol Sci 2024;25(1):524.
[13] Samdani SK, Kishore J, Yogi V, et al. A Comparative Study of Cold Dissection Tonsillectomy and Harmonic Scalpel Tonsillectomy Under Microscope- Our Experience. Indian J Otolaryngol Head Neck Surg 2022;74(Suppl 3):5395-5403.
[14] Elmore L, Minissale NJ, Israel L, et al. Evaluating the Healing Potential of J-Plasma Scalpel-Created Surgical Incisions in Porcine and Rat Models. Biomedicines 2024;12(2):277.
[15] Belloso A, Chidambaram A, Morar P, et al. Coblation tonsillectomy versus dissection tonsillectomy: Postoperative hemorrhage. Laryngoscope 2003;113(11):2010-2013.
[16] Parab SR, Khan MM. Endoscope holder-assisted endoscopic coblation tonsillectomy. Eur Arch Oto-rhino-l 2020;277(11):3223-3226.
[17] Chen L, Xie L, Wu T, et al. An experimental study on low-temperature plasma tissue ablation and its thermal effect. J Phys D Appl Phys 2024;57(36):365202.
[18] Xiao A, Liu D, He D, et al. Plasma Scalpels: Devices, Diagnostics, and Applications. Biomedicines 2022;10(11):2967.
[19] Guo J, Wang Y, Liu H, et al. Thermal–Electrical Optimization of Lithium-Ion Battery Conductor Structures Under Extreme High Amperage Current. Appl Sci 2025;15(10):5338.
[20] Trieschmann J, Vialetto L, Gergs T. Review: Machine learning for advancing low-temperature plasma modeling and simulation. arXiv 2023;arXiv:2307.00131.
[21] Wiechmann EP, Morales AS, Aqueveque P, et al. Three-Dimensional FEM Thermal and Electrical Analysis of Copper Electrowining Intercell Bars. IEEE Trans Ind Appl 2017;53(1):638-644.
[22] Cicciù M. Bioengineering Methods of Analysis and Medical Devices: A Current Trends and State of the Art. Materials (Basel) 2020;13(3):797.
[23] Panchal B, Bhadauria A, Varghese S. 3D FEM Simulation and Analysis of Fractal Electrode-Based FBAR Resonator for Tetrachloroethene (PCE) Gas Detection. Fractal Fract 2022;6(9):491.
[24] Stawarz JE, Matteini L, Parashar TN, et al. Comparative Analysis of the Various Generalized Ohm's Law Terms in Magnetosheath Turbulence as Observed by Magnetospheric Multiscale. J Geophys Res Space Physics 2021;126(1):2020JA028447.
[25] Tungjitkusolmun S, Staelin ST, Haemmerich D, et al. Three-dimensional finite-element analyses for radio-frequency hepatic tumor ablation. IEEE Trans Biomed Eng 2002;49(1):3-9.
[26] Qasem NAA, Generous MM, Qureshi BA, et al. A Comprehensive Review of Saline Water Correlations and Data: Part II—Thermophysical Properties. Arab J Sci Eng 2021;46(3):1941-1979.
[27] Generous MM, Qasem NAA, Qureshi BA, et al. A Comprehensive Review of Saline Water Correlations and Data-Part I: Thermodynamic Properties. Arab J Sci Eng 2020;45(11):8817-8876.
[28] Fic A, Białecki RA, Kassab AJ. Solving Transient Nonlinear Heat Conduction Problems by Proper Orthogonal Decomposition and the Finite-Element Method. Numer Heat Tr B-Fund 2005;48(2):103-124.
[29] Babich L, Loĭko TV. Generalized Paschen's Law for Overvoltage Conditions. IEEE Trans

Plasma Sci 2016;44(12):3243-3248.
[30] Škoro N, Marić D, Malović G, et al. Electrical Breakdown in Water Vapor. Phys Rev E Stat Nonlin Soft Matter Phys 2011;84(5 Pt 2):055401.
[31] Shih T-C, Huang H-W, Wei W-C, et al. Parametric analysis of effective tissue thermal conductivity, thermal wave characteristic, and pulsatile blood flow on temperature distribution during thermal therapy. Int J Heat Mass Transfer 2014;52:113-120.
[32] Shih T-C, Horng T-L, Huang H-W, et al. Numerical analysis of coupled effects of pulsatile blood flow and thermal relaxation time during thermal therapy. Int J Heat Mass Transfer 2012;55(13):3763-3773.
[33] Schutt DJ, Haemmerich D. Sequential Activation of a Segmented Ground Pad Reduces Skin Heating During Radiofrequency Tumor Ablation: Optimization via Computational Models. IEEE Trans Biomed Eng 2008;55(7):1881-1889.